ELSEVIER

Contents lists available at ScienceDirect

# Journal of Luminescence

journal homepage: www.elsevier.com/locate/jlumin



# Full Length Article

# Light-emitting Sn-doped CsX (X=Cl, Br, I) materials prepared by mechanochemical processing

Xuan Huang <sup>a,b</sup>, Xiyu Wen <sup>c</sup>, Y. Charles Lu <sup>a,b,\*\*</sup>, Fuqian Yang <sup>a,d,\*</sup>

- <sup>a</sup> Laboratory of Functional Materials, University of Kentucky, Lexington, KY, 40506, USA
- <sup>b</sup> Department of Mechanical and Aerospace Engineering, University of Kentucky, Lexington, KY, 40506, USA
- <sup>c</sup> Center for Aluminium Technology, University of Kentucky, Lexington, KY, 40506, USA
- <sup>d</sup> Materials Program, Department of Chemical and Materials Engineering, University of Kentucky, Lexington, KY, 40506, USA

# ARTICLE INFO

#### Keywords: Sn-doped CsX Mechanochemical process Photoluminescence Photoresponse Stability

#### ABSTRACT

The success in synthesizing light-emitting lead-based halide perovskites from cesium halides (CsX, X: I, Br, and Cl) has stimulated great interests in the applications of halide perovskites and in the development of lead-free halide perovskites and related light-emitting materials. In this work, we explore the feasibility of synthesizing Sn-doped CsX powders (microcrystals) via mechanochemical processing and investigate the optical characteristics of the prepared Sn-doped CsX powders. The prepared Sn-doped CsX powders emit light with ultra-wide emission peak under UV light of 365 nm in wavelength, which is attributed to self-trapped exciton emission. The emission peak intensity decreases with the increase in temperature in the Sn-doped CsXs due to thermal quenching. The characterization of the optoelectronic response of the prepared Sn-doped CsX powders reveals that the current intensity passing through the Sn-doped CsX powders decreases with the increase of the intensity of the incident white light under the same applied voltage. Light emitting diodes are constructed from the prepared Sn-doped CsX powders and exhibit an ultra-wide spectrum spanning the range of entire visible light. The method presented in this provides a simple technique to prepare light-emitting materials of Sn-doped CsXs via mechanochemical process.

### 1. Introduction

The progress in the solution-based synthesis of inorganic and organic-inorganic lead-based halide perovskites has stimulated great interests in the applications of halide perovskites in a variety of areas, including imaging and energy conversion [1–7]. In the heart of the applications of lead-based halide perovskites are the tunable optical characteristics through the control of crystal size and chemical composition. However, the applications and commercialization of lead-based halide perovskites have been hindered by the concerns on the lead toxicity from the degradation products [8–10] to the earth and human health as well as on the use of hazardous solvents, such as dimethylformamide (DMF) and/or dimethyl sulfoxide (DMSO), in the preparation of precursor solutions. There is a great need to develop eco-friendly methods to synthesize lead-free halide perovskites for potential applications in optoelectronics and energy storage.

A variety of alternatives for the replacement of lead in lead-based

halide perovskites, including tin (Sn), copper (Cu), silver (Ag), bismuth (Bi), indium (In), antimony (Sb), and germanium (Ge), have been explored, and lead-free halide perovskites and lead-free double halide perovskites have been successfully synthesized [11–16]. Some lead-free halide perovskites and lead-free double halide perovskites have exhibited excellent optoelectronic performance and great power conversion efficiencies. However, the synthesis of the lead-free halide perovskites and lead-free double halide perovskites has relied mostly on the solution-based processes, which use DMF and/or DMSO. To mitigate the potential hazards of organic solvents to the environment and human health, mechanochemical and aqueous-based approaches have been demonstrated to produce lead-free halide perovskites and lead-free double halide perovskites.

Tang et al. used an aqueous solution to produce  $Cs_2SnCl_6$  [17] and  $Cs_2SnI_6$  [18] microcrystals, from which  $Cs_2SnCl_6$  [17] and  $Cs_2SnI_6$  [18] nanocrystals were produced under ultrasonication. Ma et al. [19] used mechanical grinding to form lead-free hybrid manganese halides of

<sup>\*\*</sup> Corresponding author. Department of Mechanical and Aerospace Engineering, University of Kentucky, Lexington, KY, 40506, USA.

<sup>\*</sup> Corresponding author. Materials Program, Department of Chemical and Materials Engineering, University of Kentucky, Lexington, KY, 40506, USA. *E-mail addresses:* ycharles.lu@uky.edu (Y.C. Lu), fuqian.yang@uky.edu (F. Yang).

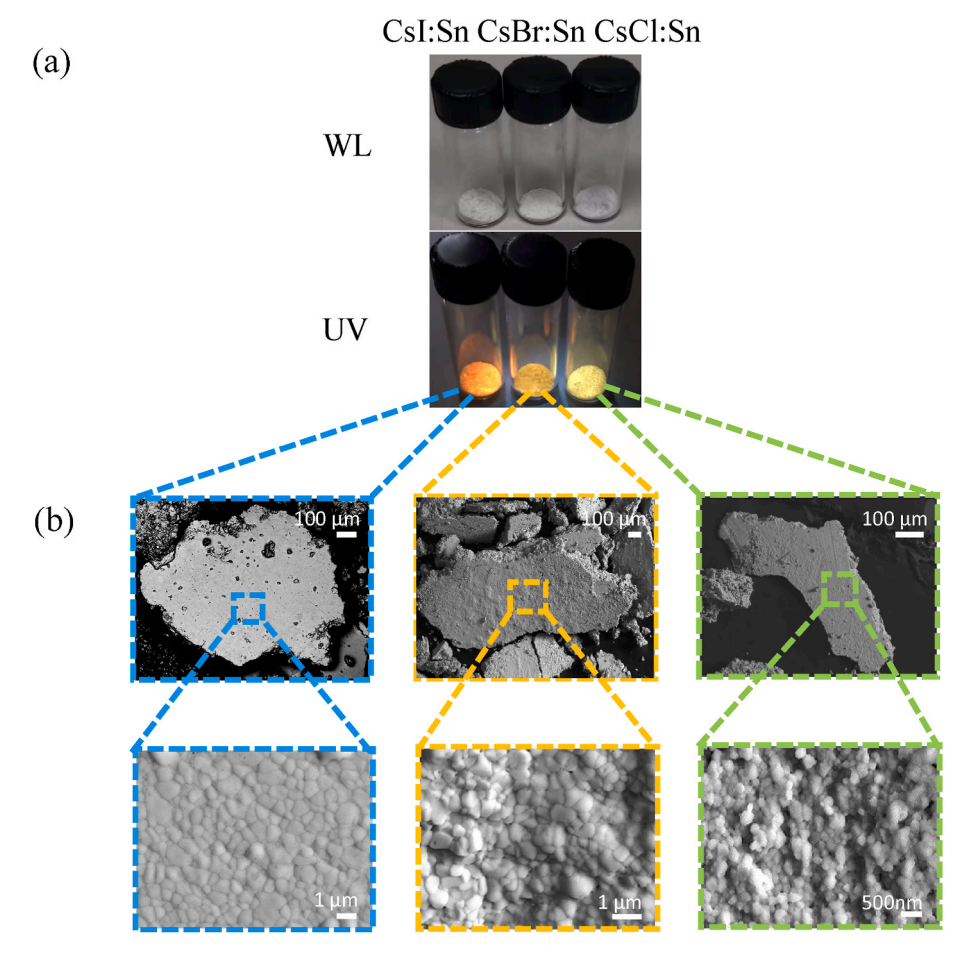


Fig. 1. (a) Optical images of the prepared Sn-doped CsXs powders (X: I, Br, and Cl) under white light and UV light of 365 nm in wavelength, and (b) SEM images of the prepared Sn-doped CsXs (X: I, Br, and Cl).

microsizes at room temperature, which exhibited green emission. Breternitz et al. [20] produced lead-free double perovskite  $Cs_2[AgIn]Br_6$  with a bandgap of 2.36 eV via a planetary ball. Using ball milling, Kumar et al. [21] prepared  $Cs_2AgBiBr_6$  nanoplates from CsBr, AgBr, and  $BiBr_3$  in a glovebox, and pointed out the dependence of crystallization on the milling time. Saski et al. [22] performed mechanochemical syntheses of  $ASnX_3$  (A = MA, FA, Cs; X = I, Br) and mixed-halide  $MASnI_xBr_{3-x}$  perovskites in a ball mill in a glovebox filled with argon, while they did not report the photoluminescence (PL) characteristics of the prepared perovskites. All these works reveal the possibility of eco-friendly producing lead-free halide perovskites using aqueous solutions and/or mechanochemical approaches.

There are reports on the light emission of CsX (X = I, Br and Cl) with the emission wavelengths centered at 310 nm and 560 nm for CsI under X-ray irradiation at room temperature [23,24], the photoluminescence centered at 3.54 eV and 4.68 eV for CsBr at 11 K under UV light of 7.75 eV, and the photoluminescence centered at 2.95 eV for CsCl at 11 K under UV light of 8.5 eV. Xu et al. [25] observed that CsBr:Zn nanocrystals exhibited light emission centered at 415 nm and 438 nm under the excitation of UV light of 360 nm in wavelength. Hawrami et al. [26] prepared CsI:Ti cuboids with the vertical Bridgeman method, and reported the light emission of the CsI:Ti cuboids at 543 nm under X-ray. Kimura et al. [27] demonstrated that CsCl:Ce transparent ceramics, which were produced through mechanical punching and thermal sintering, emitted light centered at 380 nm and 410 nm under X-ray. These results demonstrate that CsX halide compounds with and without metallic elements can emit light of different wavelengths under UV light or X-ray.

The bandgaps of CsI, CsBr, and CsCl are 3.5 [28], 4.24 [29], and 5.46

eV [30], respectively. Recently, Adhikari et al. [31] prepared a precursor solution with DMF as the solvent and 1:1 ratio of CsBr to SnBr<sub>2</sub>, and used a fluidic system to obtain Sn(II)-doped CsBr with orange emission at a wavelength of ~615 nm. Their results show that doping Sn (II) in CsBr can reduce the bandgap of CsBr and result in orange emission under the irradiation of UV light of 365 nm in wavelength and suggest that the bandgap of halides can likely be changed by doping metallic element. This work is aimed at using an environmentally conscientious mechanochemical process to dope Sn in CsX (X: I, Br and Cl) halide compounds under ambient conditions without any organic solvent and investigates the optical characteristics of the prepared Sn-doped CsXs. This approach not only represents a straightforward and eco-friendly synthesis process but also presents the promise to avoid the issues associated with the detrimental effects of organic solvents on the environment and human health.

# 2. Experiment details

The materials used in this work were CsI (99.9 %, Alfa Aesar), CsBr (99.9 %, Beantown chemical), CsCl (99.9 %, Alfa Aesar), SnI $_2$  (99 %, Strem Chemical), SnBr $_2$  (99 %, Beantown chemical), and SnCl $_2$  (99 %, Sigma Aldrich). No further purification was conducted prior to the use of the materials.

A suspension consisting of 0.04 mmol  $SnI_2$  (14.9 mg  $SnI_2$ ), 0.04 mmol  $SnBr_2$  (11.1 mg  $SnBr_2$ ), or 0.4 mmol  $SnCl_2$  (75.8 mg  $SnCl_2$ ) and 3 mL DI water was prepared in a vial and stirred under 120 rpm at 40 °C for 30 min. A mixture with 0.4 mmol CsX (104 mg for  $CsI_2$ ; 85.1 mg for  $CsI_3$ ; and 67.3 mg for  $CsI_2$ ) and 10  $\mu$ L of the corresponding suspension (1.33  $\times$  10<sup>-4</sup> mmol of  $SnI_2$  and  $SnBr_2$ ; 13.33  $\times$  10<sup>-4</sup> mmol of  $SnCl_2$ ) was

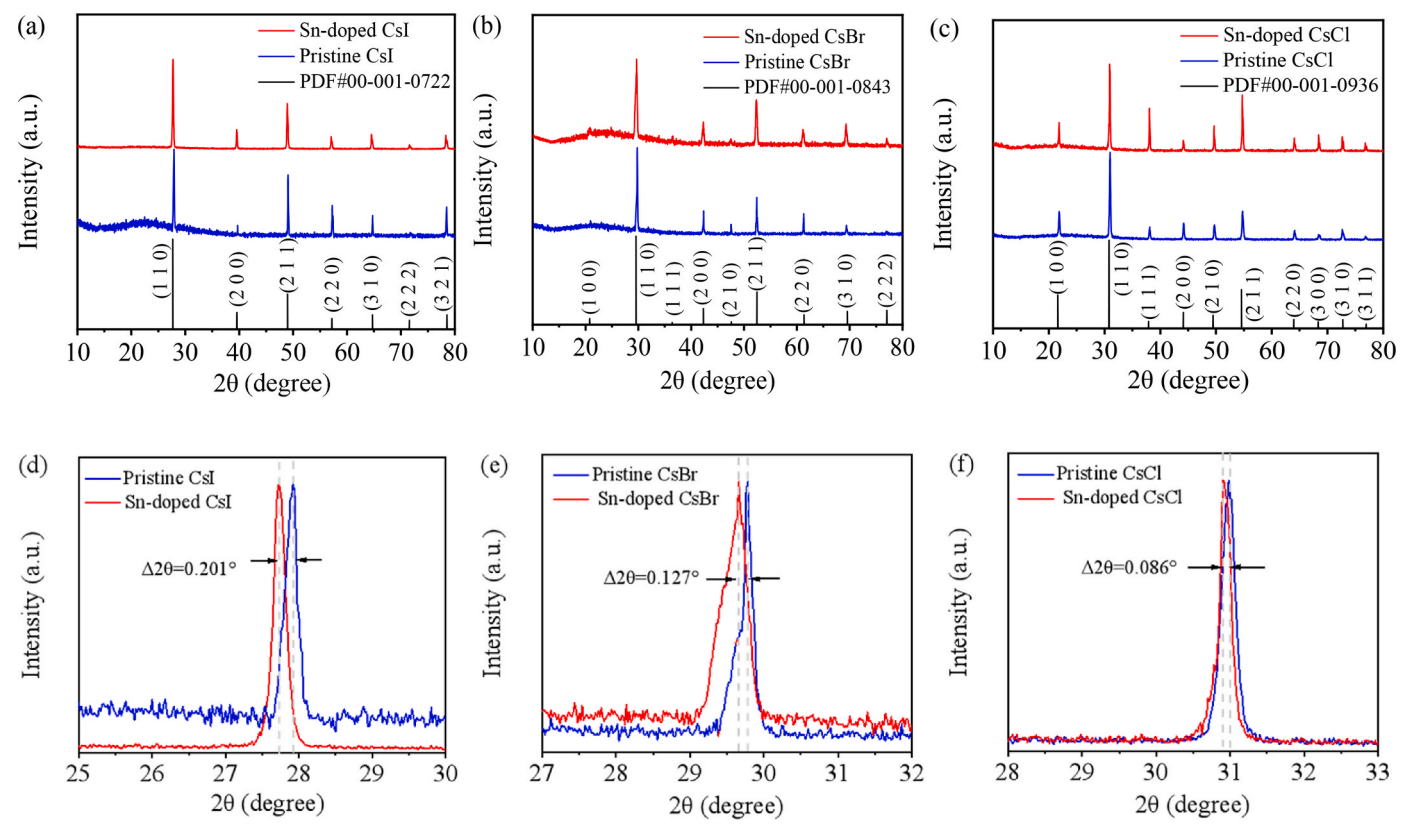


Fig. 2. XRD patterns of the prepared Sn-doped CsI powders (a, d), Sn-doped CsBr powders (b, e), and Sn-doped CsCl powders (c, f).

placed in a ceramic mortar. Mechanical grinding of the mixtures of CsI + SnI $_2$ , CsBr + SnBr $_2$ , and CsCl + SnCl $_2$  for 10 min,  $5\times10$  min, and 10 min, respectively, at 19  $^{\circ}$ C and a relative humidity of 22 % led to the formation of Sn-doped CsX powders with commendable light emission. Note that the preparation of Sn-doped CsBr powders is slightly different from the other two. Briefly, after the first 10 min grinding, an additional 10  $\mu L$  of the suspension of SnBr $_2$  was added to the ground materials for further grinding. Such a process was repeated four times, i.e., the total grinding lasted 5  $\times$  10 min. The Sn-doped CsX (X: I, Br and Cl) powders of 0.4 mmol were deposited onto a glass substrate, which was then placed on the top of a commercial LED (light-emitting diode) of 3 W in power and 365 nm in wavelength to form simple LEDs.

The crystal structures of the Sn-doped CsX powders were analyzed on an X-ray diffractometer (XRD) (Bruker D8 Discover) with a radiation of  $\text{CuK}_{\alpha}\,(\lambda=1.5406\,\text{Å}).$  The morphologies and chemical constituents of the Sn-doped CsX powders were imaged and analyzed, respectively, on a scanning electron microscope (SEM) (JEOL JSM-5900lLV) equipped with an energy-dispersive X-ray spectroscope (EDS).

The PL characteristics of the Sn-doped CsX powders were analyzed on a spectrometer (Ocean Optics) under a UV light of 365 nm in wavelength. The absorbance spectra of the Sn-doped CsX powders were acquired on a UV–Visible spectrophotometer (EVOLUTION 201). The photoresponse of the Sn-doped CsX powders was characterized, using a Keithley 2400 power meter (SMU instrument) and a 150 W fiber optic dual gooseneck illuminator (B&B Microscopes LTD).

# 3. Computational details

The bandgaps of Sn-doped CsX halide compounds were numerically calculated, using Quantum ESPRESSO [32] of a plane-wave quantum simulation code. For Sn-doped CsI, a supercell consisting of 8 CsI atoms and 1 interstitial Sn atom was constructed with 4.04 Å in the Cs–I interatomic distance. For Sn-doped CsBr, a supercell consisting of 36 CsBr atoms and 1 interstitial Sn atom was constructed with 3.80 Å in the

Cs–Br interatomic distance. For Sn-doped CsCl, a supercell consisting of 36 CsCl atoms and 1 interstitial Sn atom was constructed with 3.59  $\rm \mathring{A}$  in the Cs–Cl interatomic distance.

#### 4. Results

Fig. 1 presents optical and SEM images of the prepared Sn-doped CsI, Sn-doped CsBr, and Sn-doped CsCl powders. According to Fig. 1a, all the Sn-doped CsX (X: I, Br, and Cl) powders are white under white light, and exhibit orange-light emission for the Sn-doped CsI powders, yellow-light emission for the Sn-doped CsBr powders, and light green-light emission for the Sn-doped CsCl powders under the UV light of 365 nm in wavelength. The yellow-light emission of the Sn-doped CsBr powders is different from the orange-light emission of the submicron Sn-doped CsBr crystals reported by Adhikari et al. [31]. The reason for the difference in the light emission is unclear and might be due to the difference in the use of solvent. Adhikari et al. [31] used DMF as the solvent in the preparation of the precursor solution, while we used DI water in the mechanochemical synthesis. As pointed out by Tang et al. [18], the emission wavelength of a semiconductor is dependent on the thermodynamic state of the semiconductor, including size, stress, and surrounding material. The mechanical grounding and the use of DI water during the mechanochemical synthesis of the Sn-doped CsBr powders likely introduced different stress state in the Sn-doped CsBr powders as well as different surrounding material from the ones formed by the fluidic system [31], which results in the difference in the emission wavelength [33]. Also, the size of the Sn-doped CsBr powders produced in this work is larger than the ones reported by Adhikari et al. [31].

The SEM images shown in Fig. 1b reveal the plate-like structures of the prepared Sn-doped CsXs powders, as expected, due to the shear and compression during the mechanical grinding. The enlarged views point to that the plate-like structures consist of an aggregation of micron and sub-micron particles. From the SEM images, we determine the size distributions of the prepared Sn-doped CsXs powders. Fig. S1 in

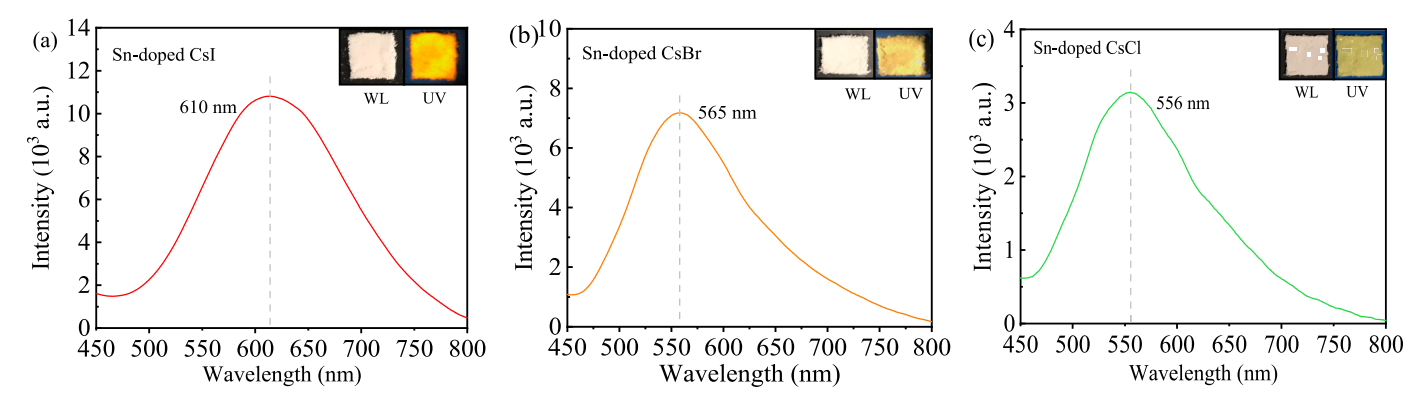


Fig. 3. PL spectra of the prepared Sn-doped CsI powders (a), Sn-doped CsBr powders (b), and Sn-doped CsCl powders (c). The insets are optical images of the Sn-doped CsXs powders (X: I, Br, and Cl) under white light and UV light (365 nm in wavelength), respectively.

Supplementary Information depicts the size distributions of the prepared Sn-doped CsXs powders, which span from 100 nm to 1.4  $\mu$ m for the Sn-doped CsI powders, from 200 nm to 900 nm for the Sn-doped CsBr powders, and from 100 nm to 500 nm for the Sn-doped CsCl powders. Such differences in the particle sizes are likely due to the differences in the solubilities of CsI, CsBr, and CsCl in water, which are 848 g/L, 1230 g/L, and 1910 g/L at 25 °C, respectively. The larger the solubility, the easier the disintegration, and the smaller the particle sizes. Therefore, the Sn-doped CsCl powders have the smallest particle sizes.

Fig. S2 in Supplementary Information presents the EDS mappings of the prepared Sn-doped CsX powders. In general, the mechanical grinding of the mixtures led to uniform distribution of Sn in the prepared Sn-doped CsX powders. Using the EDS spectra in Fig. S3 in Supplementary Information, the molar ratio of Cs to X is found to be approximately 1:1, indicating the doping of Sn in the CsX powders during the mechanochemical processing.

Fig. S4 in Supplementary Information shows the XPS spectra of the prepared Sn-doped CsX powders. The binding energy of Sn-3d $_{5/2}$  for Sn-doped CsI is 485.6 eV which is in accord with 485.8 eV of Sn (II) in CsSnI $_3$  and less than 486.81 eV of Sn (IV) in Cs $_2$ SnI $_6$  reported by Zhang et al. [34]; the binding energy of Sn-3d $_{5/2}$  for Sn-doped CsBr is 486.3 eV in accord with 486.6 eV of Sn (II) in Sn-doped CsBr reported by Bingol et al. [31]; and the binding energy of Sn-3d $_{5/2}$  for Sn-doped CsCl is 485.5 eV, which is in accord with 485.6 eV of Sn (II) in CsSnCl $_3$  [35] and less than 487.0 eV of Sn (IV) in Cs $_2$ SnCl $_6$  reported by Zhang et al. [36]. The slight difference of the binding energies of Sn 3d5/2 between the Sn-doped CsCl (485.5 eV) and CsSnCl $_3$  (485.6 eV) can be likely attributed to the difference in the thermodynamic states of Sn. The grinding introduces internal stress in the Sn-doped CsCl powders, and CsSnCl $_3$  is at a stress "free" state. Also, the coordination number of Sn in the Sn-doped CsCl is likely different from that in CsSnCl $_3$ .

Fig. 2 illustrates the differences of XRD patterns between pristine cesium salts and the prepared Sn-doped ones from respective mixtures. The red lines represent the XRD patterns of the prepared Sn-doped ones, and the blue lines represent the XRD patterns of the corresponding pristine cesium salts. The XRD pattern of the pristine CsI matches well with the ICDD card of PDF#00-001-0722 for cubic CsI (Fig. 2a). For the Sn-doped CsI, the XRD peaks centered at 27.7°, 39.5°, 48.9°, 57.1°, 64.5°, 71.6°, and 78.3° correspond to (110), (200), (211), (220), (310), (222), and (321) crystal planes of cubic CsI, respectively. There is a left shift of the XRD peak of the (110) plane with 0.201° in 2θ for the Sn-doped CsI, compared with the XRD peak of the (110) plane of the pristine CsI. According to Bragg's law

$$n\lambda = 2d\sin\theta \tag{1}$$

with n as the diffraction order,  $\lambda$  as the diffraction wavelength, d as the interplanar spacing, and  $\theta$  as the diffraction angle, the left shift of the XRD peak suggests the increase in the interplanar spacing of the

corresponding crystal plane. Thus, doping Sn in CsI causes the increase of the interplanar spacing of the (110) plane of the CsI, as expected. The increase of the interplanar spacing of the (110) plane of the CsI is found to be  $2.2 \times 10^{-3}$  nm for n=1.

The XRD pattern of the pristine CsBr matches well with the ICDD card of PDF#00-001-0843 for cubic CsBr (Fig. 2b). For the Sn-doped CsBr, the XRD peaks centered at  $20.7^{\circ}$ ,  $29.6^{\circ}$ ,  $36.6^{\circ}$ ,  $42.3^{\circ}$ ,  $47.5^{\circ}$ ,  $52.3^{\circ}$ ,  $61.2^{\circ}$ ,  $69.3^{\circ}$ , and  $77.0^{\circ}$  correspond to (100), (110), (111), (200), (210), (211), (220), (310), and (222) crystal planes of cubic CsBr, respectively. There is a  $0.127^{\circ}$  left shift of  $2\theta$  for the XRD peak centered at  $29.6^{\circ}$  from the pristine CsBr to the Sn-doped CsBr, as shown in Fig. 2e, in a similar trend to the Sn-doped CsI. The left shift again suggests that doping Sn in CsBr leads to the increase of the interplanar spacing of the (110) plane of the CsBr. The increase of the interplanar spacing of the (110) plane of the CsBr is found to be  $1.2 \times 10^{-3}$  nm for n=1.

The XRD patterns of the pristine CsCl presented in Fig. 2c matches well with the ICDD card of PDF#00-001-0936 for cubic CsCl. For the Sndoped CsCl, the XRD peaks centered at 21.8°, 30.9°, 38.0°, 44.1°, 49.7°, 54.7°, 64.0°, 68.4°, 72.7°, and 76.8° correspond to (100), (110), (111), (200), (210), (211), (220), (300), (310), and (311) crystal planes of cubic CsCl, respectively. There is a 0.084° left shift of 2 $\theta$  for the XRD peak centered at 30.9° from the pristine CsCl to the Sn-doped CsCl, as shown in Fig. 2f, in a similar trend to the Sn-doped CsI and CsBr. The left shift again suggests that doping Sn in CsCl leads to the increase of the interplanar spacing of the (110) plane of the CsCl. The increase of the interplanar spacing of the (110) plane of the CsCl is found to be  $7 \times 10^{-4}$  nm for n=1.

It should be pointed out that the change in the interplanar spacing is dependent on the crystal structure and bonding strength of the material. It also depends on the atomic fraction of dopant presented in the material.

Fig. 3a–c depicts the PL spectra of the prepared Sn-doped CsX powders prepared with 0.4 mmol CsI in a  $10~\mu L$  SnI $_2$  solution, 0.4 mmol CsBr in  $5\times(10~\mu L$  SnBr $_2$  solution), and 0.4 mmol CsCl in a  $10~\mu L$  SnCl $_2$  solution, respectively. All the PL spectra exhibit ultra-wide emission peak, which is the characteristic of self-trapped exciton (STE) emission. Thus, the prepared Sn-doped CsX powders can be categorized as STE emission materials [37]. The PL peaks are centered at 610 nm (2.03 eV), 565 nm (2.19 eV), and 556 nm (2.23 eV) for the Sn-doped CsI powders, Sn-doped CsBr powders, and Sn-doped CsCl powders, respectively. The corresponding FWHMs (full width at half maximum) are 515.75 meV, 478.83 meV, and 565.40 meV for the Sn-doped CsI powders, Sn-doped CsBr powders, and Sn-doped CsCl powders, respectively. The smallest FWHM is 478.83 meV for the Sn-doped CsBr powders, suggesting that the Sn-doped CsBr powders possess the least variation in powder sizes among the three prepared Sn-doped CsX powders.

Following the same process, we prepared Sn-doped CsX powders by adding the same amount (10  $\mu$ L) of the SnX2 suspension in the ceramic

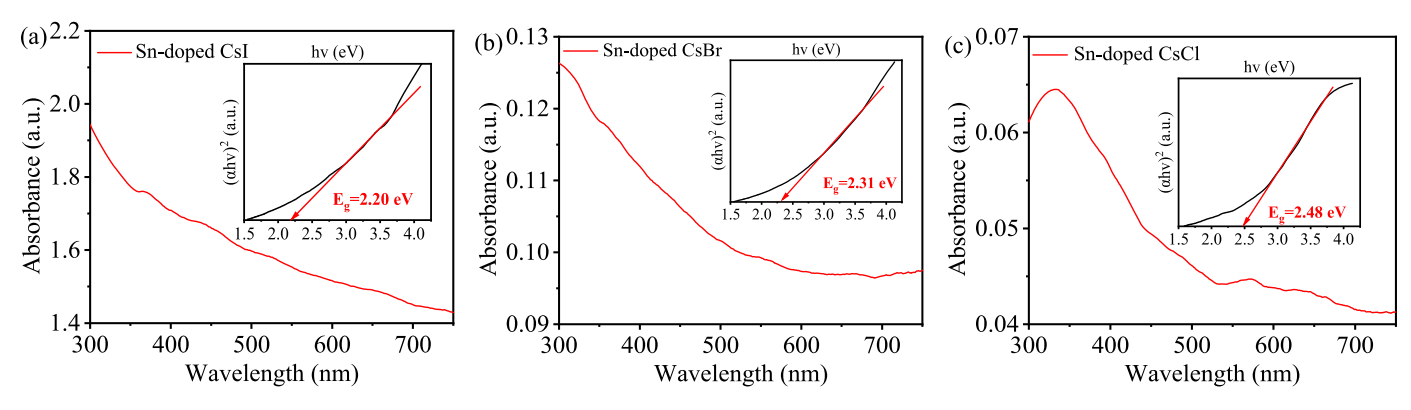


Fig. 4. Absorbance spectra of the prepared Sn-doped CsI powders (a), Sn-doped CsBr powders (b), and Sn-doped CsCl powders (c). The insets are Tauc plots of the corresponding Sn-doped CsX powders.

mortar after each grinding multiple times. Let "N" be the times of the same amount of the  $SnX_2$  suspension used to prepare the Sn-doped CsX powders. Fig. S5 in Supplementary Information presents the PL spectra of the Sn-doped CsX powders with different Ns. It is evident that the PL

peaks of the prepared Sn-doped CsX powders are independent of the total amount of the mixture of CsX and the  $SnX_2$  suspension used in the manual grinding. The emission intensities of the prepared Sn-doped CsI and Sn-doped CsCl compounds decrease with increasing number (N) of

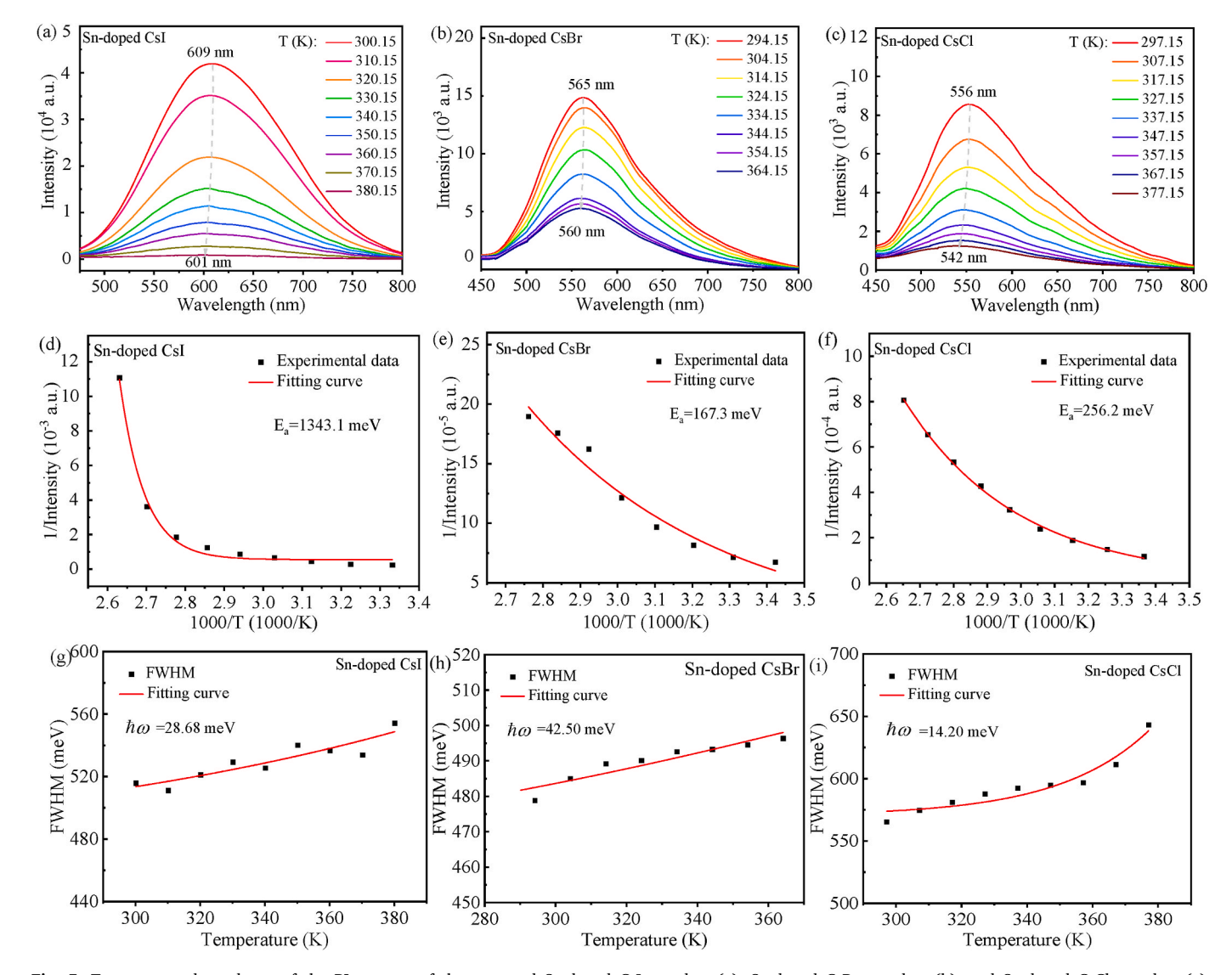


Fig. 5. Temperature-dependence of the PL spectra of the prepared Sn-doped CsI powders (a), Sn-doped CsBr powders (b), and Sn-doped CsCl powders (c); temperature-dependence of the PL peak intensities of the PL spectra of the prepared Sn-doped CsI powders (d), Sn-doped CsBr powders (e), and Sn-doped CsCl powders (f); and temperature-dependence of the FWHMs of the PL spectra of the prepared Sn-doped CsI powders (g), Sn-doped CsBr powders (h), and Sn-doped CsCl powders (i).

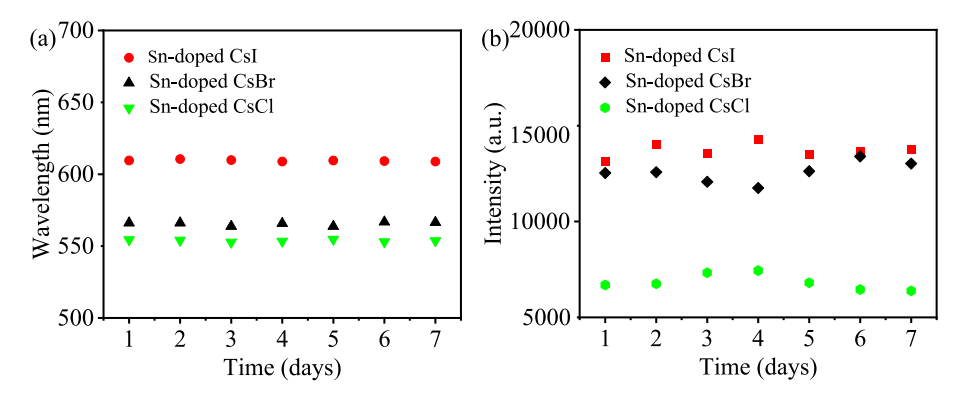


Fig. 6. Temporal variations of the PL peak wavelength and PL peak intensity over a period of 7 days for the prepared Sn-doped CsX powders: (a) PL peak wavelength, and (b) PL peak intensity.

adding the same amount of the  $\mathrm{SnX}_2$  suspension in the ceramic mortar, while the emission intensity of the prepared Sn-doped CsBr compound increases with increasing number (N) of adding the same amount of the  $\mathrm{SnBr}_2$  suspension in the ceramic mortar. The mechanism for the opposite trend of the variation of the emission intensity of the Sn-doped CsBr compound with the number (N) to the Sn-doped CsI and Sn-doped CsCl compounds is unclear. It might be associated with the difference in the solubilities of Sn in CsX compounds. Adding more SnBr suspension during the grinding for N less than or equal to 5 causes more Sn to move into non-doped CsBr compound, leading to the increase in the emission intensity of the prepared Sn-doped CsBr compound. Note that the emission intensity of the prepared Sn-doped CsBr compound decreases with increasing number (N) for N > 6, as shown in Fig. S5d.

To examine if solvent plays a role in the light emission of the ground mixtures, we used isopropyl alcohol as the sole solvent in the grounding of the mixtures under the same conditions as the corresponding ones with DI water as the sole solvent. The ground mixtures of  $CsI + SnI_2$  and  $CsCl + SnCl_2$  do not emit light under UV light of 365 nm. We further used a mixture of DI water and isopropyl alcohol in a 1:1 vol ratio as the solvent in the grounding of the mixtures under the same conditions. Fig. S6 in Supplementary Information shows the PL spectra of the ground mixtures formed with the mixture of DI water and isopropyl alcohol as the solvent. It is evident that the ground mixtures of  $CsI + SnI_2$  and  $CsCl + SnCl_2$  emitted light under the UV light of 365 nm with the emission peak wavelength the same as the corresponding ones prepared with DI water as the solvent. For the ground mixture of  $CsBr + SnBr_2$ , there is a blue shift of 21 nm, compared to the corresponding one prepared with DI water as the solvent. These results likely reveal that solvent plays an important role in the light emission of the ground mixtures.

Fig. 4a–c presents the absorbance spectra of the prepared Sn-doped CsX powders. Using the absorbance spectra, we construct Tauc plots

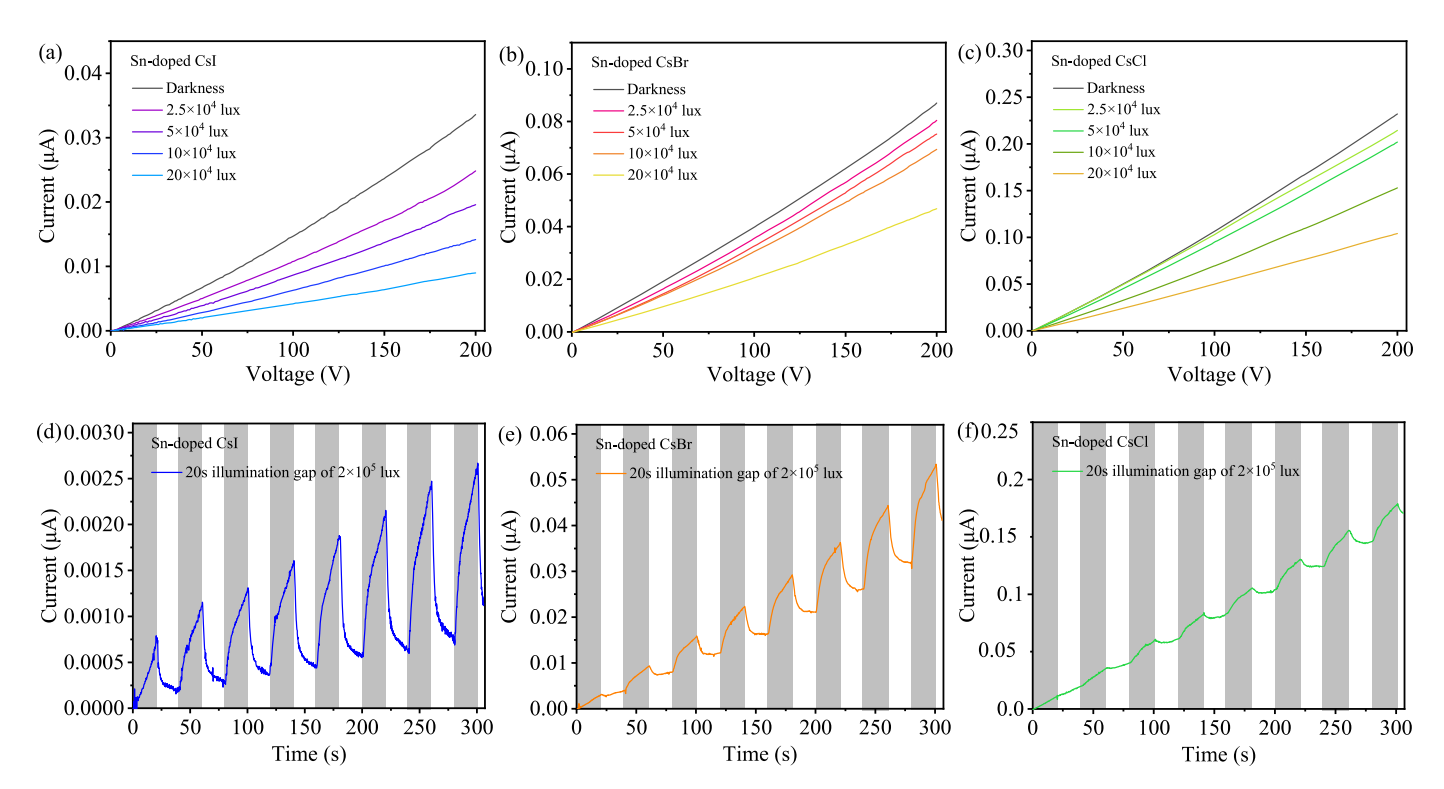


Fig. 7. I–V curves of the prepared Sn-doped CsX powders with 0.8 mmol CsX under different luminous intensities of white light: (a) Sn-doped CsI powders, (b) Sn-doped CsBr powders, and (c) Sn-doped CsCl powders. I–V curves of the prepared Sn-doped CsX powders under periodic irradiation of white light of  $2 \times 10^5$  lux in luminous intensity and a voltage sweeping at a constant rate of 200 V/306.8 s with the largest voltage of 200 V: (a) Sn-doped CsI powders, (b) Sn-doped CsBr powders, and (c) Sn-doped CsCl powders. (Gray columns represent the dark condition, and white columns represent the illumination under white light of  $2 \times 10^5$  lux in luminous intensity.)

and present the Tauc plots as an inset in the corresponding figures. From the Tauc plots, the bandgaps of the prepared Sn-doped CsX powders are calculated to be 2.20 eV, 2.31 eV, and 2.48 eV for the Sn-doped CsI powders, Sn-doped CsBr powders, and Sn-doped CsCl powders, respectively, which are larger than the corresponding ones of 2.03 eV, 2.19 eV, and 2.23 eV. The large Stokes shift between the bandgap from the absorbance measurement and the optical bandgap from the PL measurement is the STE characteristic, supporting that the light emission of the prepared Sn-doped CsX powders is controlled by the STE emission.

Fig. 5a–c displays the PL spectra of the prepared Sn-doped CsX powders at different temperatures under the UV light of 365 nm in wavelength. The peak intensity of the emission light of the prepared Sn-doped CsX powders decreases with the increase of temperature. The peak wavelength of the emission light exhibits blue shifts of 609 nm at 300.15 K to 601 nm at 380.15 K for the Sn-doped CsI powders, 565 nm at 294.15 K to 560 nm at 364.15 K for the Sn-doped CsBr powders, and 556 nm at 297.15 K to 542 nm at 377.15 K for the Sn-doped CsCl powders. Such a decreasing trend for the temperature dependence of the peak wavelength of the emission light is similar to that of inorganic halide perovskites.

Using the data shown in Fig. 5a–c, the temperature dependencies of the peak intensity and the PL FWHM of the emission light under UV light of 365 nm in wavelength are presented in Fig. 5d–f and Fig. 5g–I, respectively. It is evident that the peak intensity of the emission light exhibits a nonlinear decreasing trend with the increase of temperature and the PL FWHM exhibits an increasing trend with the increase of temperature. In general, the decrease of the peak intensity of emission light can be attributed to that increasing temperature increases the probability of the non-radiative recombination losses, associated with the redistribution of carriers into various energy levels. Also, increasing temperature can enhance electron–phonon interactions, leading to the increase in the PL FWHM of emission light.

The long-term optical stability of the prepared Sn-doped CsX powders was examined at ambient conditions for a period of 7 days. Fig. S7 in Supplementary Information depicts the PL spectra of the prepared Sndoped CsX powders over the period. From Fig. S7, the temporal variations of both the PL peak wavelength and PL peak intensity of the prepared Sn-doped CsX powders are determined and presented in Fig. 6. It is evident that there are no observable changes of the PL peak wavelength of the Sn-doped CsX powders. The PL peak intensities fluctuate in the range of 13161 and 14291 for the Sn-doped CsI powders, 11751 to 13398 for the Sn-doped CsBr powders, and 6383 to 7442 for the Sndoped CsCl powders. The fluctuation in the intensity of the emission light might be due to the slight differences in the location and/or intensity of the excitation light of 365 nm in wavelength between different measurements. In general, the prepared Sn-doped CsX powders exhibited excellent long-term stability over a period of 7 days under ambient conditions.

The photoresponses of the prepared Sn-doped CsX powders with 0.8 mmol CsX were examined under white light, using the structure shown in Fig. S8 in Supplementary Information. Fig. 7a–c presents the I–V curves of the prepared Sn-doped CsX powders under different luminous intensities of white light, whose PL spectrum is depicted in Fig. S9 in Supplementary Information. In general, the electric current is a nonlinearly increasing function of the applied voltage, suggesting the nonlinear conducting characteristic of the prepared Sn-doped CsX powders. It is interesting to note that the electric current decreases with the increase of the intensity of the white light under the same applied electric voltage. The mechanism for such behavior is unclear and might be associated with light-induced heating, which increases the scattering of electrons and causes the increase in the resistance to the motion of electrons.

Fig. 7d–f presents the I–V curves under periodic changes between a dark environment and a white light environment of  $2\times 10^5$  lux in luminous intensity for the prepared Sn-doped CsX powders under the voltage sweeping at a constant rate of 200 V/306.8 s with the largest

voltage of 200 V. The time for each interval was 20 s. From Fig. 7d–f, we note that exposing the Sn-doped CsX powders to white light caused the drop of the electric current immediately and switching to the dark environment led to the increase of the electric current immediately for all the three Sn-doped CsX powders, which is qualitatively in accord with the results shown in Fig. 7a–c. For the same time interval, the prepared Sn-doped CsI powders exhibited the largest change in the electric current and the prepared Sn-doped CsCl powders exhibited the smallest change in the electric current. Such results are in consistence with the trend shown in Fig. 7a–c.

#### 5. Discussion

The temperature dependence of the PL peak intensity of the emission light of a semiconductor under UV light can be expressed as [38].

$$I(T) = \frac{I_0}{1 + Ae^{(-E_a/k_BT)}}$$
 (2)

where  $I_0$  is the PL peak intensity at 0 K,  $E_a$  is the nominal activation energy,  $k_B$  is the Boltzmann constant, A is a constant, and T is the absolute temperature. Using Eq. (2) to fit the data shown in Fig. 5d–f, we obtain the nominal activation energies of 1343.1, 106.3, and 256.2 meV for the Sn-doped CsI powders, Sn-doped CsBr powders, and Sn-doped CsCl powders, respectively. For comparison, the fitting curves are included in the corresponding figures. It is evident that Eq. (2) describes well the temperature dependence of the PL peak intensity of the emission light. Such large nominal activation energies suggest that the decrease of the PL peak intensity with the increase of temperature is attributed to thermal quenching.

The configuration-coordinate model has been used to describe the STE emission of semiconductors. According to the configuration-coordinate model, the temperature dependence of the FWHM of STE emission,  $\Gamma(T)$ , can be described as [39–42].

$$\Gamma(T) = \Gamma(0) \sqrt{\coth\left(\frac{\hbar\omega}{2k_B T}\right)}$$
(3)

with  $\Gamma(0)$  as the half-line width at 0 K and  $\hbar$   $\omega$  as the phonon energy. Using Eq. (3) to fit the data shown in Fig. 5g–i, we obtain the half-line widths at 0 K and the phonon energies as (459.43, 28.68), (465.93, 42.50), and (400.26, 14.20) in the units of (meV, meV) for the Sn-doped CsI powders, Sn-doped CsBr powders, and Sn-doped CsCl powders, respectively. For comparison, the fitting curves are included in the corresponding figures. It is evident that Eq. (3) describes well the temperature dependence of the PL FWHM of the emission light.

From the half-line width at 0 K, the Huang-Rhys factor, *S*, which is the mean number of phonons emitted in absorption, can be calculated from the following equation [43].

$$S = \left(\frac{\Gamma(0)}{2.36\hbar\omega}\right)^2 \tag{4}$$

Using the fitting results of  $\Gamma(0)$  and  $\hbar$   $\omega$ , we obtain the Huang-Rhys factor as 46.1, 21.6, and 142.6 for the Sn-doped CsI powders, Sn-doped CsBr powders, and Sn-doped CsCl powders, respectively. The large numerical values of the Huang-Rhys factor are in good accord with the general condition for STE emission [44]. This result confirms that the physical process for the light emission of the prepared Sn-doped CsX powders under the UV light of 365 nm in wavelength is controlled by the STE emission. The highest phonon energy,  $\hbar$   $\omega$ , for the Sn-doped CsBr powders suggests that the Sn-doped CsBr powders exhibited the largest emission of photons under the same conditions. The smallest Huang-Rhys factor for the Sn-doped CsBr powders suggests that the Sn-doped CsBr powders experienced the least recombination of excited electrons and holes during the excitation process.

We performed the first principles calculations to analyze the effect of

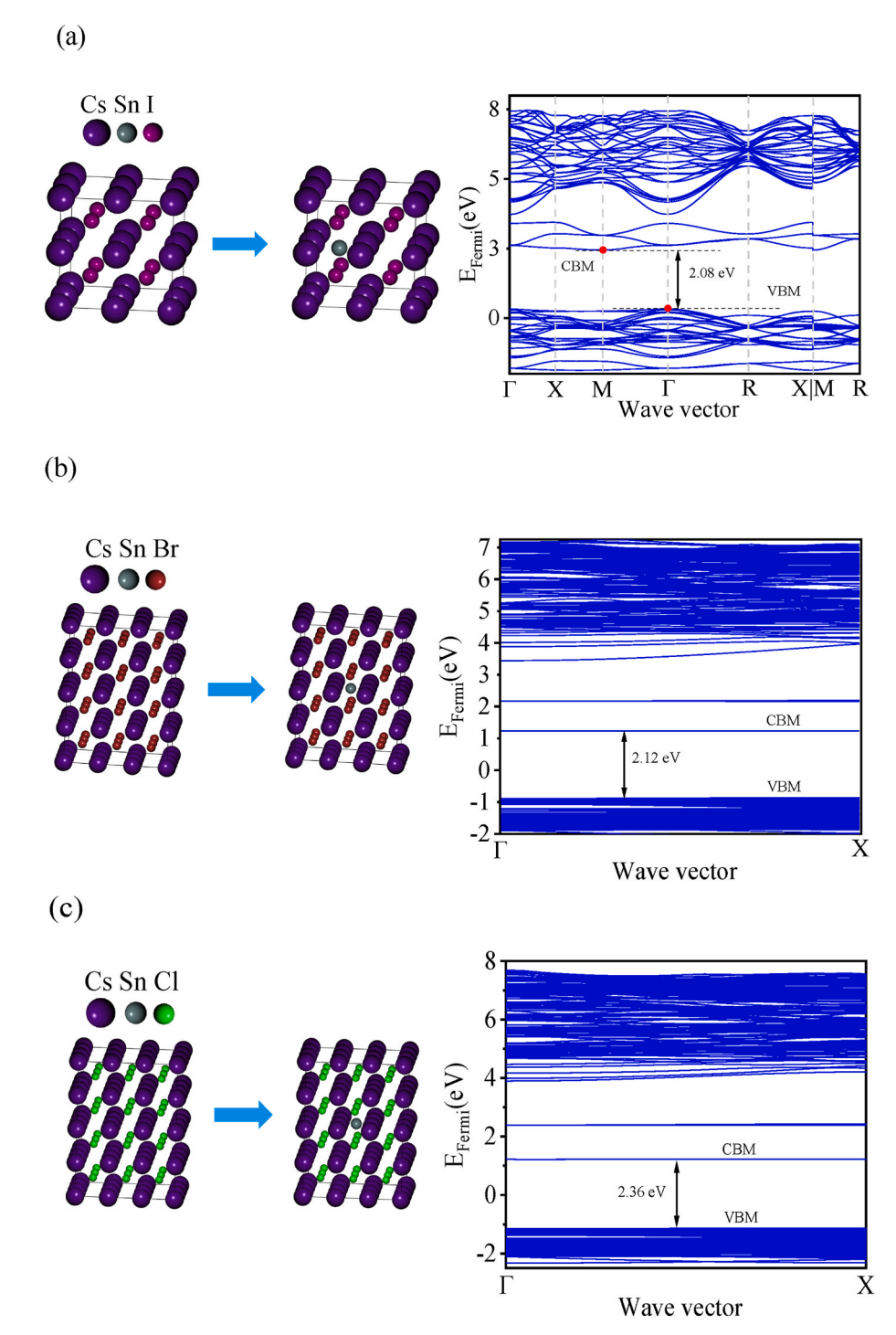


Fig. 8. Changes of the crystal structures of CsXs to Sn-doped CsXs, supercells and bond structures of Sn-doped CsXs: (a) Sn-doped CsI with Sn at a tetragonal site, (b) Sn-doped CsBr with Sn at an orthorhombic site, and (c) Sn-doped CsCl with Sn at an orthorhombic site.

Sn-doping on the bandgaps of CsX (X: I, Br, and Cl) halide compounds, using Quantum ESPRESSO [32] of a plane-wave quantum simulation code. Fig. 8 presents the changes of the crystal structures of CsXs to Sn-doped CsXs, the supercells of Sn-doped CsX halide compounds and the corresponding band structures. Note that the limited power of the computer made it very difficult to perform the DFT calculation for Sn-doped CsX lattices with more than 36 atoms/ions.

The interatomic distances of the Sn-doped CsXs are 4.04 Å for Cs–I, 3.80 Å for Cs–Br, and 3.59 Å for Cs–Cl. The angles of the supercells are  $\alpha=\beta=\gamma=90^\circ.$  From the band structures, we obtain indirect bandgap of 2.08 eV for the Sn-doped CsI, direct bandgap of 2.12 eV for the Sn-doped

CsBr, and direct bandgap of 2.36 eV for the Sn-doped CsCl. The wavelengths corresponding to the bandgaps of 2.08, 2.23, and 2.36 eV are 597, 584, and 525 nm, respectively, which exhibit a decreasing trend qualitatively in accord with the trend of the PL peak wavelengths for the Sn-doped CsXs (X: I, Br, and Cl), as observed in the experimental study. The first principles calculations qualitatively support the experimental observation that doping Sn doping in CsXs (X: I, Br, and Cl) reduces the bandgap of the corresponding pristine CsXs.

Considering the potential applications of the prepared Sn-doped CsX powders in lighting and displays, we prepared simple light emitting diodes (LEDs) from the prepared Sn-doped CsX powders. Briefly, 0.4

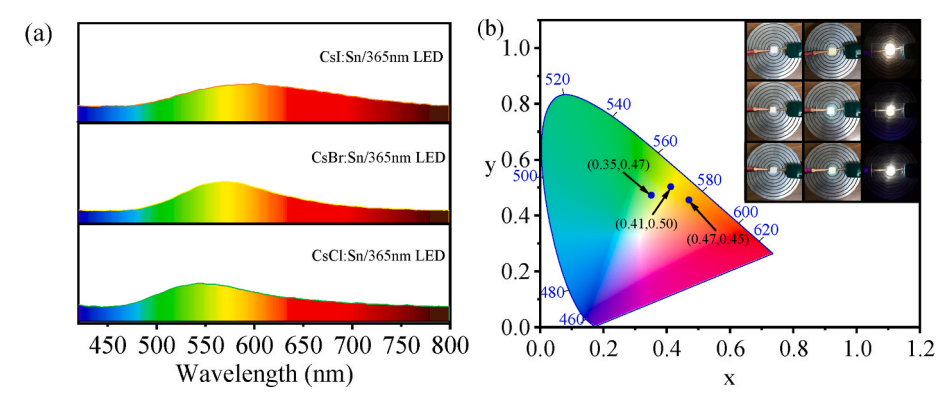


Fig. 9. (a) PL spectra, and (b) CIE diagram of the LEDs made from the Sn-doped CsI powders, Sn-doped CsBr powders, and Sn-doped CsCl powders, respectively. The insets display turn-on/turn-off photographs of the Sn-doped CsI/365 nm LED (first line), Sn-doped CsBr/365 nm LED (second line), and Sn-doped CsCl/365 nm LED (third line).

mmol of Sn-doped CsXs (X = Cl, Br, I) powders were coated on the surface of a glass substrate, respectively, which was then placed on the top of an LED of 365 nm in wavelength. The prepared LEDs exhibited an ultra-wide spectrum spanning the range of entire visible light, as shown in Fig. 9a. The optical micrographs embedded in Fig. 9b show the lighting of the LEDs at 400 mA, as required by the LED of 365 nm in wavelength. Transforming the PL data to the CIE diagram, the corresponding coordinates are (0.47, 0.45), (0.41, 0.50), and (0.35, 0.47) for the LEDs made from the Sn-doped CsI powders, Sn-doped CsBr powders, and Sn-doped CsCl powders, respectively. Such results suggest that the Sn-doped CsX powders have the potential for applications in lighting.

#### 6. Conclusions

In summary, we have demonstrated the facile method of forming Sndoped CsX (X: I, Br, and Cl) halide powders via mechanochemical processing under ambient conditions. The XRD analyses have revealed the increase in the interplanar spacing of the (110) plane of the CsXs with the presence of Sn, which validates the formation of Sn-doped CsX halide powders. The prepared Sn-doped CsX powders emit light with the PL peak wavelengths of 610, 565, and 556 nm for the Sn-doped CsI powders, Sn-doped CsBr powders, and Sn-doped CsCl powders, respectively, under UV light of 365 nm in wavelength. The physical process for the light emission of the prepared Sn-doped CsX powders is the selftrapped exciton emission, as evidenced ultra-wide emission peak and supported by the large numerical values of the Huang-Rhys factor from the analysis of the temperature dependence of the PL and FWHM of the emission light. The thermal quenching controls the temperature dependence of the PL peak intensity of the prepared Sn-doped CsX powders. We have performed the first principles calculations of the band structures of Sn-doped CsX halide compounds and obtained the bandgaps qualitatively in consistence with the corresponding ones obtained from the PL measurements.

The I–V behavior of the prepared Sn-doped CsX powders exhibited nonlinear characteristics; exposing the prepared Sn-doped CsX powders to white light led to the decrease in the electric current under the same applied voltage. Using the prepared Sn-doped CsX powders, we have constructed simple LEDs. The PL spectra of the LEDs exhibited an ultrawide spectrum spanning the range of entire visible light. These results suggest that the Sn-doped CsX powders have the potential for applications in lighting. This study provides a simple avenue for developing light-emitting materials of Sn-doped CsX materials via mechanochemical process, which have potential applications in lighting and display technologies.

#### CRediT authorship contribution statement

Xuan Huang: Formal analysis, Data curation, Investigation, Methodology, Writing – original draft. Xiyu Wen: Investigation, Visualization. Y. Charles Lu: Funding acquisition, Resources, Supervision, Writing – review & editing. Fuqian Yang: Writing – review & editing, Validation, Supervision, Project administration, Methodology, Investigation, Funding acquisition, Formal analysis.

## Declaration of competing interest

The authors declare that they have no known competing financial interests or personal relationships that could have appeared to influence the work reported in this paper.

# Data availability

Data will be made available on request.

# Acknowledgments

FY is grateful for the support by the NSF through the grant CBET-2018411 monitored by Dr. Nora F Savage.

# Appendix A. Supplementary data

Supplementary data to this article can be found online at https://doi.org/10.1016/j.jlumin.2024.120614.

## References

- [1] J. Jeong, M. Kim, J. Seo, H. Lu, P. Ahlawat, A. Mishra, Y. Yang, M.A. Hope, F. T. Eickemeyer, M. Kim, Y.J. Yoon, I.W. Choi, B.P. Darwich, S.J. Choi, Y. Jo, J. H. Lee, B. Walker, S.M. Zakeeruddin, L. Emsley, U. Rothlisberger, A. Hagfeldt, D. S. Kim, M. Grätzel, J.Y. Kim, Pseudo-halide anion engineering for α-FAPbI<sub>3</sub> perovskite solar cells, Nature 592 (2021) 381–385.
- [2] H. Wang, X. Zhang, Q. Wu, F. Cao, D. Yang, Y. Shang, Z. Ning, W. Zhang, W. Zheng, Y. Yan, S.V. Kershaw, L. Zhang, A.L. Rogach, X. Yang, Trifluoroacetate induced small-grained CsPbBr<sub>3</sub> perovskite films result in efficient and stable light-emitting devices, Nat. Commun. 10 (2019) 665.
- [3] R. Gonzalez-Rodriguez, E. Hathaway, H. Paulette, J.L. Coffer, Y. Lin, J. Cui, Two-dimensional quantum-confined CsPbBr<sub>3</sub> in silicene for LED applications, ACS Appl. Nano Mater. 6 (2023) 4028–4033.
- [4] X. Li, Y. Tan, H. Lai, S. Li, Y. Chen, S. Li, P. Xu, J. Yang, All-inorganic CsPbBr<sub>3</sub> perovskite solar cells with 10.45% efficiency by evaporation-assisted deposition and setting intermediate energy levels, ACS Appl. Mater. Interfaces 11 (2019) 29746–29752.
- [5] L. Duan, H. Zhang, M. Liu, M. Grätzel, J. Luo, Phase-pure γ-CsPbI<sub>3</sub> for efficient inorganic perovskite solar cells, ACS Energy Lett. 7 (2022) 2911–2918.
- [6] L.A. Frolova, A.I. Davlethanov, N.N. Dremova, I. Zhidkov, A.F. Akbulatov, E. Z. Kurmaev, S.M. Aldoshin, K.J. Stevenson, P.A. Troshin, Efficient and stable MAPbI<sub>3</sub>-based perovskite solar cells using polyvinylcarbazole passivation, J. Phys. Chem. Lett. 11 (2020) 6772–6778.

- [7] Y. Miao, Y. Ke, N. Wang, W. Zou, M. Xu, Y. Cao, Y. Sun, R. Yang, Y. Wang, Y. Tong, W. Xu, L. Zhang, R. Li, J. Li, H. He, Y. Jin, F. Gao, W. Huang, J. Wang, Stable and bright formamidinium-based perovskite light-emitting diodes with high energy conversion efficiency, Nat. Commun. 10 (2019) 3624.
- [8] J. Li, H.-L. Cao, W.-B. Jiao, Q. Wang, M. Wei, I. Cantone, J. Lü, A. Abate, Biological impact of lead from halide perovskites reveals the risk of introducing a safe threshold, Nat. Commun. 11 (2020) 310.
- [9] S.-Y. Bae, S.Y. Lee, J.-w. Kim, H.N. Umh, J. Jeong, S. Bae, J. Yi, Y. Kim, J. Choi, Hazard potential of perovskite solar cell technology for potential implementation of "safe-by-design" approach, Sci. Rep. 9 (2019) 4242.
- [10] M. Ren, X. Qian, Y. Chen, T. Wang, Y. Zhao, Potential lead toxicity and leakage issues on lead halide perovskite photovoltaics, J. Hazard Mater. 426 (2022) 127848
- [11] N. Balachandran, T.M. Robert, T. Jayalatha, P.M. Neema, D. Mathew, J. Cyriac, Lead-free, mixed tin-copper perovskites with improved stability and optical properties, J. Alloys Compd. 879 (2021) 160325.
- [12] M. Palummo, E. Berrios, D. Varsano, G. Giorgi, Optical properties of lead-free double perovskites by ab initio excited-state methods, ACS Energy Lett. 5 (2020) 457–463.
- [13] Y. Yang, C. Liu, M. Cai, Y. Liao, Y. Ding, S. Ma, X. Liu, M. Guli, S. Dai, M. K. Nazeeruddin, Dimension-controlled growth of antimony-based perovskite-like halides for lead-free and semitransparent photovoltaics, ACS Appl. Mater. Interfaces 12 (2020) 17062–17069.
- [14] M. Miodyńska, T. Klimczuk, W. Lisowski, A. Zaleska-Medynska, Bi-based halide perovskites: stability and opportunities in the photocatalytic approach for hydrogen evolution, Catal. Commun. 177 (2023) 106656.
- [15] T. Krishnamoorthy, H. Ding, C. Yan, W.L. Leong, T. Baikie, Z. Zhang, M. Sherburne, S. Li, M. Asta, N. Mathews, S.G. Mhaisalkar, Lead-free germanium iodide perovskite materials for photovoltaic applications, J. Mater. Chem. A 3 (2015) 23829–23832.
- [16] L. Zhou, J.-F. Liao, Z.-G. Huang, J.-H. Wei, X.-D. Wang, W.-G. Li, H.-Y. Chen, D.-B. Kuang, C.-Y. Su, A highly red-emissive lead-free indium-based perovskite single crystal for sensitive water detection, Angew. Chem. Int. Ed. 58 (2019) 5277–5281.
- [17] X. Tang, X. Wen, F. Yang, Ultra-stable blue-emitting lead-free double perovskite Cs<sub>2</sub>SnCl<sub>6</sub> nanocrystals enabled by an aqueous synthesis on a microfluidic platform, Nanoscale 14 (2022) 17641–17653.
- [18] X. Tang, S. Weng, W. Hao, F. Yang, Aqueous synthesis of ultrastable dual-coloremitting lead-free double-perovskite Cs<sub>2</sub>SnI<sub>6</sub> with a wide emission span enabled by the size effect, ACS Sustain. Chem. Eng. 11 (2023) 9121–9131.
- [19] Y.-Y. Ma, Y.-R. Song, W.-J. Xu, Q.-Q. Zhong, H.-Q. Fu, X.-L. Liu, C.-Y. Yue, X.-W. Lei, Solvent-free mechanochemical syntheses of microscale lead-free hybrid manganese halides as efficient green light phosphors, J. Mater. Chem. C 9 (2021) 9952–9961.
- [20] J. Breternitz, S. Levcenko, H. Hempel, G. Gurieva, A. Franz, A. Hoser, S. Schorr, Mechanochemical synthesis of the lead-free double perovskite Cs<sub>2</sub>[AgIn]Br<sub>6</sub> and its optical properties, J. Phys.: Energy 1 (2019) 025003.
- [21] S. Kumar, I. Hassan, M. Regue, S. Gonzalez-Carrero, E. Rattner, M.A. Isaacs, S. Eslava, Mechanochemically synthesized Pb-free halide perovskite-based Cs<sub>2</sub>AgBiBr<sub>6</sub>-Cu-RGO nanocomposite for photocatalytic CO<sub>2</sub> reduction, J. Mater. Chem. A 9 (2021) 12179–12187.
- [22] M. Saski, D. Prochowicz, W. Marynowski, J. Lewiński, Mechanosynthesis, optical, and morphological properties of MA, FA, CsSnX<sub>3</sub> (X= I, Br) and phas-pure mixed-halide MASnI<sub>x</sub>Br<sub>3-x</sub> perovskites, Eur. J. Inorg. Chem. 2019 (2019) 2680–2684.
- [23] S. Kubota, S. Sakuragi, S. Hashimoto, J.-z. Ruan, A new scintillation material: pure CsI with 10 ns decay time, Nucl. Instrum. Methods Phys. Res., Sect. A 268 (1988) 275–277
- [24] V.B. Mikhailik, V. Kapustyanyk, V. Tsybulskyi, V. Rudyk, H. Kraus, Luminescence and scintillation properties of CsI: a potential cryogenic scintillator, Phys. Status Solidi 252 (2015) 804–810.

- [25] H. Xu, J. Liang, Z. Zhang, Z. Deng, Y. Qiu, M. He, J. Wang, Y. Yang, C.C. Chen, Lead-free bright blue light-emitting cesium halide nanocrystals by zinc doping, RSC Adv. 11 (2021) 2437–2445.
- [26] R. Hawrami, E. Ariesanti, A. Farsoni, D. Szydel, H. Sabet, Growth and evaluation of improved CsI:Tl and NaI:Tl scintillators, Crystals 12 (2022) 1517.
- [27] H. Kimura, F. Nakamura, T. Kato, D. Nakauchi, G. Okada, N. Kawaguchi, T. Yanagida, Scintillation and dosimetric properties of Ce:CsCl transparent ceramics, Sensor. Mater. 30 (2018) 1555.
- [28] Z. Zhang, Q. Zhao, Y. Li, X.-P. Ouyang, Electronic structure and optical properties of CsI, CsI(Ag), and CsI(TI), J. Kor. Phys. Soc. 68 (2016) 1069–1074.
- [29] MaterialsProject, https://next-gen.materialsproject.org/materials/mp-22906.
- [30] S. Bingol, B. Erdinc, H. Akkus, Electronic band structure, optical, dynamical and thermodynamic properties of cesium chloride (CsCl) from first-principles, Int. J. Simul. Multidiscip. Des. Optim. 6 (2015) A7.
- [31] S. Das Adhikari, S. Masi, C. Echeverría-Arrondo, S. Miralles-Comins, R.S. Sánchez, J.A. Fernandes, V. Chirvony, J.P. Martínez-Pastor, V. Sans, I. Mora-Seró, Continuous-flow synthesis of orange emitting Sn(II)-doped CsBr materials, Adv. Opt. Mater. 9 (2021) 2101024.
- [32] P. Giannozzi, O. Andreussi, T. Brumme, O. Bunau, M. Buongiorno Nardelli, M. Calandra, R. Car, C. Cavazzoni, D. Ceresoli, M. Cococcioni, N. Colonna, I. Carnimeo, A. Dal Corso, S. de Gironcoli, P. Delugas, R.A. DiStasio Jr., A. Ferretti, A. Floris, G. Fratesi, G. Fugallo, R. Gebauer, U. Gerstmann, F. Giustino, T. Gorni, J. Jia, M. Kawamura, H.Y. Ko, A. Kokalj, E. Küçükbenli, M. Lazzeri, M. Marsili, N. Marzari, F. Mauri, N.L. Nguyen, H.V. Nguyen, A. Otero-de-la-Roza, L. Paulatto, S. Poncé, D. Rocca, R. Sabatini, B. Santra, M. Schlipf, A.P. Seitsonen, A. Smogunov, I. Timrov, T. Thonhauser, P. Umari, N. Vast, X. Wu, S. Baroni, Advanced capabilities for materials modelling with Quantum ESPRESSO, J. Phys. Condens. Matter 29 (2017) 465901.
- [33] F.Q. Yang, Stress effect on bandgap change of a semiconductor nanocrystal in an elastic matrix, Phys. Lett. 428 (2022) 127931.
- [34] J. Zhang, S. Li, P. Yang, W. Liu, Y. Liao, Enhanced stability of lead-free perovskite heterojunction for photovoltaic applications, J. Mater. Sci. 53 (2018) 4378–4386.
- [35] M.S. Ali, S. Das, Y.F. Abed, M.A. Basith, Lead-free CsSnCl<sub>3</sub> perovskite nanocrystals: rapid synthesis, experimental characterization and DFT simulations, Phys. Chem. Chem. Phys. 23 (2021) 22184–22198.
- [36] H. Zhang, L. Zhu, J. Cheng, L. Chen, C. Liu, S. Yuan, Photoluminescence characteristics of Sn<sup>2+</sup> and Ce<sup>3+</sup>-doped Cs<sub>2</sub>SnCl<sub>6</sub> double-perovskite crystals, Materials 12 (2019) 1501.
- [37] S. Li, J. Luo, J. Liu, J. Tang, Self-trapped excitons in all-inorganic halide perovskites: fundamentals, status, and potential applications, J. Phys. Chem. Lett. 10 (2019) 1999–2007.
- [38] M. Leroux, N. Grandjean, B. Beaumont, G. Nataf, F. Semond, J. Massies, P. Gibart, Temperature quenching of photoluminescence intensities in undoped and doped GaN, J. Appl. Phys. 86 (1999) 3721–3728.
- [39] F. Pan, J. Li, X. Ma, Y. Nie, B. Liu, H. Ye, Free and self-trapped exciton emission in perovskite CsPbBr<sub>3</sub> microcrystals, RSC Adv. 12 (2022) 1035–1042.
- [40] T.G. Mack, L. Jethi, P. Kambhampati, Temperature dependence of emission line widths from semiconductor nanocrystals reveals vibronic contributions to line broadening processes, J. Phys. Chem. C 121 (2017) 28537–28545.
- [41] D. Pal, D.N. Bose, Line shape, linewidth and configuration coordinate diagram of the Cu band (1.21 eV) in InP, J. Appl. Phys. 78 (1995) 5206–5208.
- [42] S. Bhushan, M.V. Chukichev, Temperature dependent studies of cathodoluminescence of green band of ZnO crystals, J. Mater. Sci. Lett. 7 (1988) 319–321.
- [43] J.J. Markham, Interaction of normal modes with electron traps, Rev. Mod. Phys. 31 (1959) 956–989.
- [44] R.K. Dawson, D. Pooley, F band absorption in alkali halides as a function of temperature, Phys. Status Solidi 35 (1969) 95–105.